ACS Energy LETTERS
http://pubs.acs.org/journal/aelccp

LETTER

Wavelength-Dependent Ultrafast Charge Carrier Separation in the $WO_3/BiVO_4$ Coupled System

Ivan Grigioni,[†] Kevin G. Stamplecoskie,[‡] Danilo H. Jara,[§] Maria Vittoria Dozzi,[†] Aurelio Oriana,[∥] Giulio Cerullo,[∥] Prashant V. Kamat,[§] and Elena Selli*[,†]

[†]Dipartimento di Chimica, Università degli Studi di Milano, Via Golgi 19, I-20133 Milano, Italy
[‡]Department of Chemistry, Queen's University, Kingston, Ontario K7L 3N6, Canada
[§]Radiation Laboratory, University of Notre Dame, Notre Dame, Indiana 46556, United States
[∥]IFN-CNR, Department of Physics, Politecnico di Milano, Piazza Leonardo da Vinci 32, I-20133 Milano, Italy

Supporting Information

ABSTRACT: Due to its ~2.4 eV band gap, $BiVO_4$ is a very promising photoanode material for harvesting the blue portion of the solar light for photoelectrochemical (PEC) water splitting applications. In $WO_3/BiVO_4$ heterojunction films, the electrons photoexcited in $BiVO_4$ are injected into WO_3, overcoming the lower charge carriers' diffusion properties limiting the PEC performance of $BiVO_4$ photoanodes. Here, we investigate by ultrafast transient absorption spectroscopy the charge carrier interactions occurring at the interface between the two oxides in heterojunction systems to directly unveil their wavelength dependence. Under selective $BiVO_4$ excitation, a favorable electron transfer from photoexcited $BiVO_4$ to WO_3 occurs immediately after excitation and leads to an increase of the trapped holes' lifetime in $BiVO_4$. However, a recombination channel opens when both oxides are simultaneously excited, evidenced by a shorter lifetime of trapped holes in $BiVO_4$. PEC measurements reveal the implication of these wavelength-dependent ultrafast interactions on the performances of the $WO_3/BiVO_4$ heterojunction.

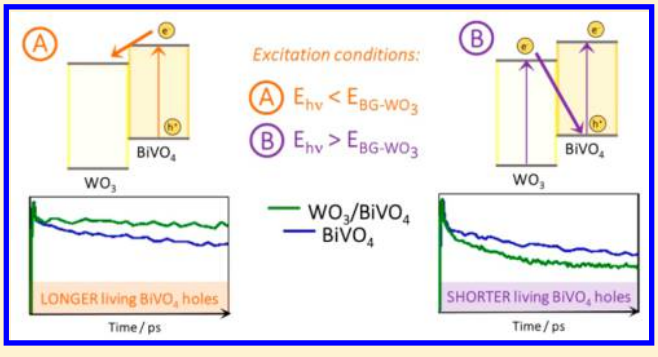

Photoelectrochemical (PEC) water splitting allows solar light conversion into chemical energy stored in hydrogen, in a fashion similar to the photosynthetic processes occurring in natural systems. In recent years, acceleration in the development of new photoactive materials led to the design of PEC devices with high solar-to-hydrogen conversion efficiencies, showing promise for large-scale commercialization in the near future.

$BiVO_4$ (BV) has rapidly emerged as one of the most promising photoanode materials for the oxygen evolution reaction.[1−3] Films prepared with state of the art synthetic procedures perform remarkably well with highly stable photocurrent densities.[4−7] When BV is combined with WO_3 in the $WO_3/BiVO_4$ (WBV) heterojunction, the excellent visible light harvesting properties of BV are combined with the superior electron conductivity of WO_3.[8,9] Due to the favorable type II band alignment between the two oxides, transfer of photoexcited electrons from the conduction band (CB) of BV to the CB of WO_3 may occur, followed by rapid diffusion to the external circuit, fostered by the higher charge mobility of WO_3. Such semiconductor oxide sensitized photoanodes allow for better spatial charge separation, consequently lowering the recombination rate of electron−hole pairs in excited BV[8,10−14] and leading to a beneficial increase of the charge carrier lifetime.[15,16]

While band alignment of the WBV heterojunction and its enhanced PEC performances when used as a photoanode suggest a charge transfer interaction, a clear understanding of the fast charge carrier dynamics following photon absorption is still elusive. Recently, the complex processes occurring in BV after band gap excitation have been investigated[17−21] on the picosecond to microsecond time scale, but the intricate charge carrier interactions occurring in heterojunction systems still wait to be fully discerned.

Here, we demonstrate, through femtosecond transient absorption (TA) measurements with tunable pump wavelength, that the ultrafast charge transfer interactions between WO_3 and

Received: March 10, 2017
Accepted: May 8, 2017
Published: May 8, 2017

DOI: 10.1021/acsenergylett.7b00216
ACS Energy Lett. 2017, 2, 1362−1367

BV in the WBV coupled system are wavelength-dependent and account for the wavelength-dependent PEC performance of the WBV heterojunction.

WO_3, BV, and WBV photoanodes were prepared by spin-coating the precursor on clean FTO, followed by annealing of the films, as detailed in the Supporting Information. Side-view FESEM images of the BV and WBV films are shown in Figure 1A,B, respectively. The heterojunction WBV film exhibits a more uniform BV coating over the underlying WO_3 with respect to the BV film directly coated on FTO because the asperities of the FTO glass are completely overshadowed by the mesoporous WO_3 layer, formed by the aggregation of small grains with an average ~17 nm diameter.[20]

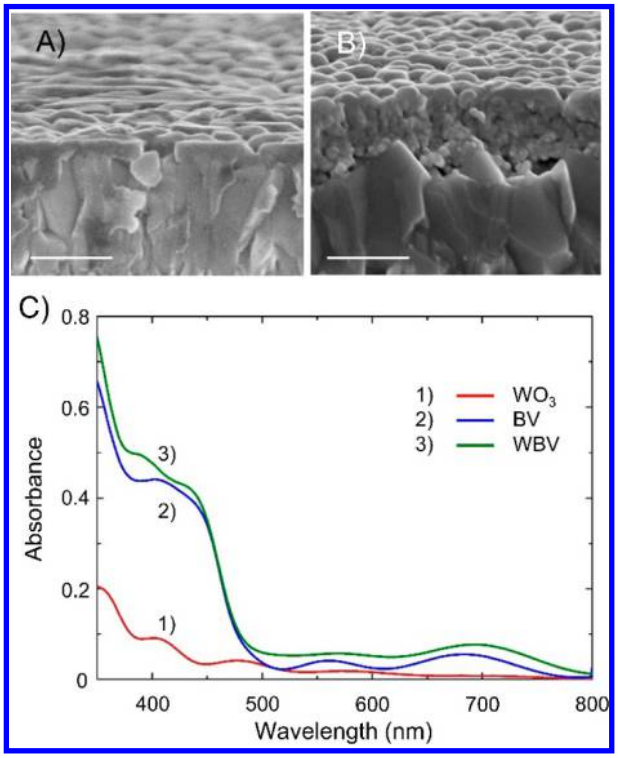

Figure 1. FESEM side-view images of (A) the BV and (B) the WBV photoanodes, obtained by coating the FTO conductive glass substrate with a BV layer or with a WO_3 layer and a BV layer, respectively. The scale bar is 500 nm. (C) Absorption spectra of the (1) WO_3 (180 nm thick), (2) BV (75 nm thick), and (3) WBV (180 nm thick WO_3 and 75 nm thick BV) films.

The absorption spectra of the WO_3, BV, and WBV films are shown in Figure 1C. In the WBV coupled system, the extremely transparent WO_3 film is effectively sensitized up to 520 nm by the BV coating. The procedure employed here to prepare BV films through spin-coating deposition of several successive layers is very reproducible, as testified by the similar absorption profiles of the BV and WBV electrodes.

The thickness of the BV layer in the BV electrode was determined from the SEM cross-sectional images shown in Figure S2 by subtracting the thickness of the FTO layer from the thickness of the overall FTO/BV. The BV coating was 75 nm thick in both BV and WBV films, which in fact exhibit identical absorbance at 420 nm, the absorption maximum of BV.

X-ray powder diffraction patterns recorded with the three films are shown in Figure S3. The patterns fit well with monoclinic (JCPDS 05-0363 for WO_3)[11,22] and monoclinic scheelite (JCPDS 75-1867 for BV)[23] structures, respectively.

Figure 2A shows the TA spectra recorded 16 ps after excitation of the BV film with a 387 nm laser pulse (20−120 μJ cm^{-2} pump fluence). A broad photoinduced absorption (PA, $\Delta A > 0$) band is observed, peaking at 470 nm and extending in the whole visible range. This signal is attributed to trapped holes in BV.[17,20,24] Ground-state depopulation due to photoexcitation leads to a photobleaching (PB, $\Delta A < 0$) band, peaking at 420 nm, which overlaps with the PA band. As shown in the inset of Figure 2A, the TA signal is linear with the pump fluence over a range from 20 to 120 μJ cm^{-2}. The same trend holds also for PB tracked at 420 nm (see Figure S4).

Figure 2B shows the dynamics of the PA signal at 470 nm, ascribed to trapped holes, as well as the fitting trace. On a 20 ps time scale, the signal shows a fast buildup (inset of Figure 2B), followed by a biexponential decay. The three processes were ascribed to the charge carrier dynamics depicted in Figure S5.[18] After charge carrier generation, first, holes diffuse and get trapped at surface states, with a time constant τ_{tr}; then, they undergo a decay process, tentatively attributed to recombination with CB electrons (τ_1) or with trapped electrons (τ_2).

Thus, the ΔA data were fit to a biexponential decay model, according to eq 1

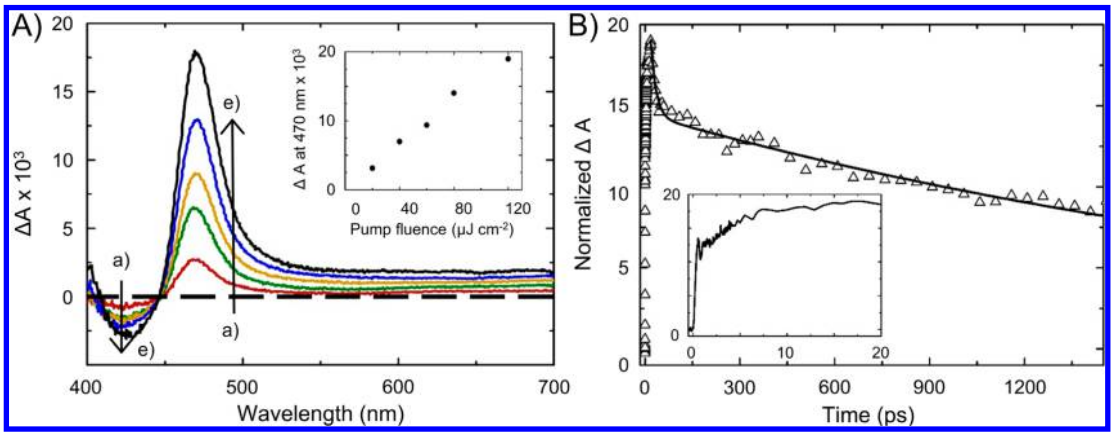

Figure 2. (A) TA spectra recorded under 387 nm excitation of the BV film with a (a) 20, (b) 40, (c) 60, (d) 80, and (e) 120 μJ cm^{-2} pump fluence. (Inset) Plot of the ΔA maxima at 470 nm vs the pump fluence. (B) Transient ΔA profile recorded at 470 nm at the highest pump fluence (triangles) and the fitting trace according to eq 1 (solid line). (Inset) Signal buildup on the 20 ps time scale.

DOI: 10.1021/acsenergylett.7b00216
ACS Energy Lett. 2017, 2, 1362−1367

$$\Delta A_{\text{decay}} = A_1 e^{-t/\tau_1} + A_2 e^{-t/\tau_2} + \Delta A_0 \quad (1)$$

where τ_1 and τ_2 are the lifetimes of the faster and slower decay processes, respectively, A_1 and A_2 are the weighted coefficients representing the contribution of each of the two processes to the overall decay, and ΔA_0 is an offset (set to zero in the fitting). Because the time constant for hole trapping is substantially fluence-independent in the studied range (see the ΔA buildup in Figure S6) and it occurs at a much higher rate than hole recombination, we fitted only the ΔA decay and ignored the buildup of the TA signal.

The fitting parameters are reported in Table S1, while Figure S7 shows an example of a fitting trace with the three processes of hole trapping (τ_{tr}), followed by fast (τ_1) and slow (τ_2) ΔA decay. Upon photoexcitation with a 20 μJ cm^{-2} fluence, 34% of the trapped holes recombine through the fast process, while for higher fluences, the contribution of the fast decay decreases to ~26%. This variation might be related to a fluence-dependent penetration depth of the pump. The time constants of both processes are unaffected by the pump fluence and are $\tau_1 \approx 22$ ps and $\tau_2 \approx 3$ ns.

Then, we studied the charge carrier interactions between the two oxides in the WBV coupled system and compared the TA dynamics in BV electrodes with that observed with the WBV heterojunction film. Because WO_3 electrodes do not give a detectable TA signal over the studied time scale,[20] BV accounts for the whole TA spectra in these two photoanode configurations. We exploited pump pulse tunability in order to excite BV selectively, or both semiconductors simultaneously, by tuning across the WO_3 band gap. We used pump wavelengths of 500 and 387 nm, that is, with energies lower or higher than the WO_3 band gap, and also at 460 nm, which is close to the WO_3 absorption edge. For each pump wavelength, we adjusted the fluence according to the sample absorption in order to obtain the same density of photoexcited carriers. The normalized TA vs time decays at 470 nm obtained upon exciting the two systems with the three pump wavelengths are shown in Figure 3, while the parameters obtained by fitting the decay traces according to eq 1 are reported in Table 1.

When the pump wavelength was tuned to 500 nm to selectively excite BV (Figure 3A), the long component of the trapped hole decay became significantly longer in the WBV system. Excluding the fast decay process, which accounts for ~19% of the holes recombined over the investigated time scale, the ΔA signal remains substantially unchanged in WBV and only ~5% of the overall signal decays through the slow process. Although such slow decay is almost beyond the limit of our femtosecond TA time window, we estimate that the time constant of the slow recombination process τ_2 increases from ~5 ns in BV to ~22 ns in WBV (Table 1). Thus, the overall recombination between electrons and holes becomes slower when BV is selectively excited in the coupled system because of the injection of photoexcited electrons from the CB of BV into the CB of WO_3. Our femtosecond TA experiments thus provide direct evidence for improved charge separation in the WBV heterojunction.

By tuning the excitation to a shorter wavelength, the lifetime of trapped holes in the heterojunction film decreases. For 460 nm excitation (see Figure 3B), the BV and WBV systems show almost identical decay dynamics. Similar results are obtained using a 450 nm pump, as shown in Figure S8. When the excitation wavelength is tuned to 387 nm, both oxide layers get excited and we observe that trapped holes in the WBV system

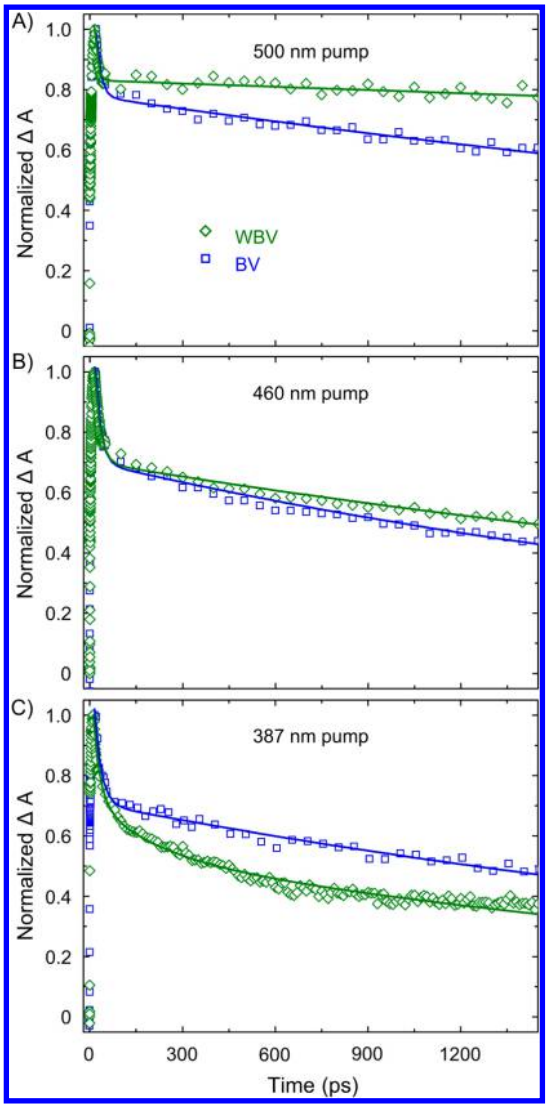

Figure 3. Dependence on the pump wavelength of the normalized TA signal recorded at 470 nm in BV and WBV films (blue squares and green diamonds, respectively). The three pump wavelengths were (A) 500, (B) 460, and (C) 387 nm.

recombine faster than in BV alone, Figure 3C. The faster TA decay suggests that a new recombination process dominates when both oxides in the heterojunction are simultaneously photoexcited.

Our femtosecond TA measurements demonstrate that the lifetime of trapped holes in the WBV heterojunction system is wavelength-dependent, as a consequence of the different processes involved. The interfacial charge interactions occurring between the two oxides in WBV heterojunction photoanodes are sketched in Figure 4. In the coupled system, when BV is selectively excited with a 500 nm pump, electron injection from the CB of BV to the CB of WO_3, with a time constant indicated as τ_{inj} in Figure 4, leads to effective spatial charge separation and to the increase of the trapped holes' lifetime (Figure 3A). However, 387 nm photons have energy greater than the band gap of WO_3 and excite both semiconductors. The shorter-lived trapped holes found in the WBV electrode after excitation at 387 nm indicate that a new recombination channel is active, that is, the recombination between photoexcited electrons in the WO_3 CB and photogenerated holes in BV (τ_r in Figure 4).

DOI: 10.1021/acsenergylett.7b00216
ACS Energy Lett. 2017, 2, 1362−1367

Table 1. Fitting Parameters, According to Equations 1 and 2, of the ΔA Transient Decay Tracked at 470 nm upon Excitation of the BV and WBV Films at Different Wavelengths and Fluences[a]

	$BiVO_4$				$WO_3/BiVO_4$					
pump (nm)	A_1	τ_1 (ps)	A_2	τ_2 (ns)	A_1	τ_1 (ps)	A_2	τ_2 (ns)	A_r	τ_r (ps)
500	0.22	16 ± 1	0.78	5.2 ± 0.2	0.18	9 ± 1	0.82	22 ± 2		
460	0.31	18 ± 1	0.69	2.9 ± 0.1	0.31	20 ± 1	0.69	4.1 ± 0.1		
387	0.27	24 ± 2	0.73	3.06 ± 0.13	0.26	24	0.56	3.06	0.18	190 ± 20

[a]Fluences: 40, 250, and 5000 μJ cm^{-2}, respectively, for 387, 460, and 500 nm pumps.

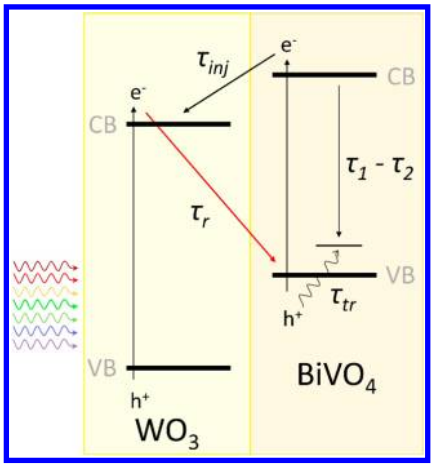

Figure 4. Electron transfer pathways involving BV and WO_3 in the heterojunction system. Processes occurring in BV: hole relaxation and trapping (τ_{tr}) and recombination between trapped holes and CB electrons (τ_1) or trapped electrons (τ_2). τ_{inj} refers to the injection of photoexcited electrons from the CB of BV to the CB of WO_3, τ_r refers to recombination due to the interfacial electron transfer from the CB of WO_3 to the valence band (VB) of BV.

An additional potential decay pathway is the backward transfer to the valence band (VB) of BV of the electrons injected from the CB of BV into the CB of WO_3. This process should take place in the coupled system also upon BV excitation at 500 nm. However, the slower ΔA decay found in WBV films (Figure 3A) evidences that the rate of such a decay pathway is slow in comparison to that of the other charge recombination paths. Therefore, in the coupled WBV system, the main process accounting for the faster recombination observed upon 387 nm excitation consists of the recombination of electrons promoted in the CB of WO_3 with the holes in the VB of BV (Figure 3C).

The contribution of this process to the overall recombination can be quantified by fitting the normalized TA time trace recorded upon excitation of the WBV system with the 387 nm pump, according to eq 2

$$\Delta A_{decay} = A_1 e^{-t/\tau_1} + A_2 e^{-t/\tau_2} + A_r e^{-t/\tau_r} + \Delta A_0 \quad (2)$$

where τ_1 and τ_2 are the time constants of the fast and slow decay processes typical of BV, respectively, and τ_r accounts for the new decay process introduced by the presence of WO_3; A_1, A_2, and A_r are the weighted contributions of each decay process to the overall decay, and ΔA_0 is an offset (set to zero in the fitting). Also in this case we fitted only the decay trace after the end of the hole trapping process. The presence of a third decay channel is evidenced by the TA dynamics of WBV in Figure 3C (see also Figure S9), which cannot be fitted by a simple biexponential decay.

By assuming that the hole recombination processes occurring in BV are not affected by the presence of WO_3, when fitting the ΔA data obtained with WBV, we constrained the τ_1 and τ_2 parameters to the values previously extracted from the kinetic analysis performed with BV. The τ_r and A_r parameters determined in this way are reported in Table 1. The newly opened charge recombination channel accounts for ∼20% of the overall hole recombination in BV, and we obtain τ_r = 190 ± 20 ps, in between the τ_1 and τ_2 values, as expected from the ΔA traces reported in Figure 3C.

Noteworthy, the results of the femtosecond TA experiments are consistent with the overall PEC performance of the WBV system. The photoanodes were characterized by performing voltammetry measurements in 0.5 M Na_2SO_4 solution (pH 7) and recording the incident photon to current efficiency (IPCE) spectra at 1.23 V vs RHE. Figure 5A shows the current densities of the WO_3, BV, and WBV electrodes as a function of the applied bias. The WBV electrode outperforms the two individual materials as a consequence of the better charge carrier extraction from the coupled system. The IPCEs of the three electrodes, traces 1, 2, and 3 in Figure 5B, confirm that the higher photocurrents shown in Figure 5A for the WBV system are due to enhanced conversion efficiencies over the entire BV absorption spectrum.

To investigate the link between the wavelength-dependent lifetime of trapped holes in BV and the PEC performance of the coupled system, in Figure 5B, we compare the IPCE values of the heterojunction electrode to those obtained with the single WO_3 and BV photoanodes by means of the IPCE enhancement factor calculated according to eq 3

$$IPCE_{enhancement} = IPCE_{WO_3/BiVO_4} - (IPCE_{WO_3} + IPCE_{BiVO_4}) \quad (3)$$

where $IPCE_{WO_3/BiVO_4}$ is the IPCE measured with the coupled system and $IPCE_{WO_3}$ and $IPCE_{BiVO_4}$ are the IPCEs of the two photoanodes recorded in separate experiments.

The coupled system clearly works significantly better than the two separate materials, and the synergy between the two oxides is maximized for wavelengths close or longer than the WO_3 absorption edge (450 nm). On the other hand, the IPCE enhancement is lower when the coupled system is photoexcited at shorter wavelength, and upon excitation at wavelengths below 350 nm, the WBV electrode is even less efficient than the two separate materials. This wavelength-dependent behavior can easily be accounted for on the basis of the results of our femtosecond TA experiments and of the charge carrier decay pathways outlined in Figure 4.

Furthermore, by combining the IPCE values with the absorption (A) spectra of the investigated films, we calculated the internal quantum efficiency (IQE) as IQE = $\frac{IPCE}{1-10^{-A}}$, which

DOI: 10.1021/acsenergylett.7b00216
ACS Energy Lett. 2017, 2, 1362−1367

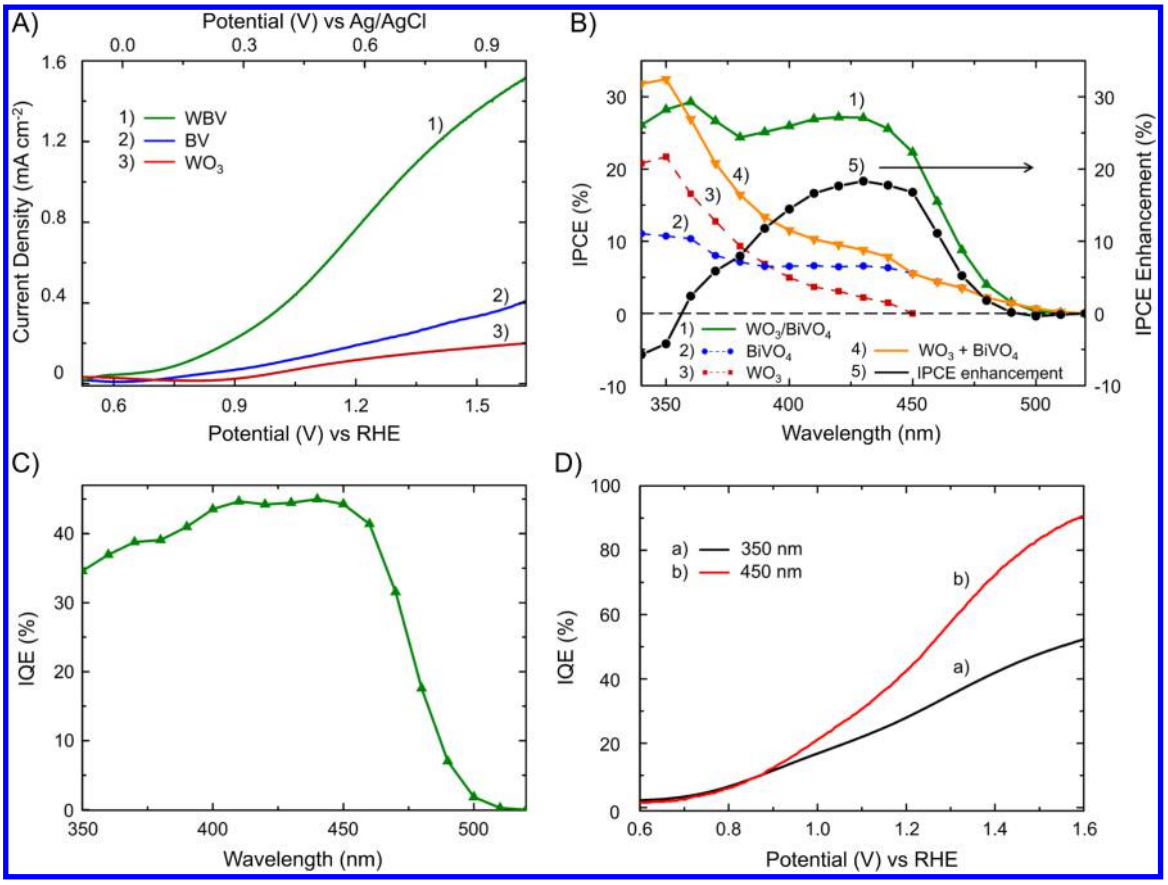

Figure 5. (A) Linear sweep voltammetry of the (1) WBV, (2) BV, and (3) WO_3 electrodes recorded with a scan rate of 10 mV s^{-1} under 1 sun AM 1.5G irradiation. (B) IPCE recorded under a 1.23 V vs RHE bias with the (1) WBV, (2) BV, and (3) WO_3 electrodes. (4) Sum of IPCE curves (2) and (3) (left axis). (5) IPCE enhancement factor of the WBV photoanode (right axis). Experiments were carried out in 0.5 M Na_2SO_4 aqueous electrolyte under back-side illumination. (C) Internal quantum efficiency (IQE) of the WBV electrode. (D) IQE as a function of the applied potential calculated from the swept IPCE reported in Figure S10 and recorded under back-side illumination by biasing a WBV photoanode from 0.6 to 1.6 V vs RHE under (a) 350 and (b) 450 nm irradiation.

accounts for the fraction of absorbed photons that actually generate photocurrent and provides information on how charge carrier recombination affects the overall performance of the WBV photoanode. Figure 5C shows that the efficiency of the coupled system in converting the charge carriers produced upon photon absorption has a maximum at 440 nm, while lower IQE values are obtained at shorter wavelengths. Indeed, upon excitation at 440 nm, 45% of the photogenerated charge carriers leads to photocurrent, which becomes only 35% for 350 nm photons. Thus, charge extraction in the WBV system increases with increasing excitation wavelength, in line with the results of our femtosecond TA investigation and of the IPCE enhancement reported in Figure 5B.

In order to understand if the applied bias in PEC measurements affects the recombination process between photoexcited electrons in the CB of WO_3 and photogenerated holes in the VB of BV (Figure 4), we finally carried out IPCE measurements with 350 and 450 nm irradiation by sweeping the applied potential (Figure S10). These experiments extend over a wider applied potential range of the IPCE measurements shown in Figure 5B, which were recorded at 1.23 V vs RHE. From these swept IPCE experiments, the corresponding swept IQE were calculated (Figure 5D). The IQE values at both wavelengths increase with increasing external bias as a consequence of the better charge separation due to band bending and formation of a depletion layer.[25] However, the IQE increase at 450 nm is larger, and the IQE at 1.6 V vs RHE under 450 nm excitation is almost twice the value determined under 350 nm excitation (Figure 5D). Thus, in the coupled system, upon excitation of both oxides at short wavelengths, the WO_3 to BV electron transfer observed in bias-free femtosecond TA experiments is active also under strong anodic polarization.

In conclusion, by exciting the WBV system at wavelengths longer than the absorption edge of WO_3, the lifetime of the holes photogenerated in BV increases because of effective charge separation due to injection of electrons from BV to WO_3. On the other hand, upon excitation of both oxides at wavelengths shorter than 450 nm, the lifetime of the holes in BV decreases because of recombination with the electrons photoexcited in WO_3. Accordingly, PEC measurements demonstrate that photocurrent generation is limited by the WO_3 to BV electron transfer occurring at short wavelengths even under a strong applied bias. This should be taken into account in the design of efficient heterojunction systems, particularly in devising photoanode architectures operating with back-side irradiation; the detrimental WO_3 to BV back electron transfer leading to recombination should be limited by engineering an electron-acceptor material with a band gap larger than that of WO_3 but having the same conductivity and proper band gap alignment with BV.

DOI: 10.1021/acsenergylett.7b00216
ACS Energy Lett. 2017, 2, 1362−1367

■ ASSOCIATED CONTENT

Supporting Information

The Supporting Information is available free of charge on the ACS Publications website at DOI: 10.1021/acsenergylett.7b00216.

Experimental: photoelectrode preparation and photoelectrochemical characterization, transient absorption spectroscopy, film thickness determination, XRPD analysis, transient absorption curves and fitting of BV films, and monochromatic swept IPCE (PDF)

■ AUTHOR INFORMATION

ORCID

Prashant V. Kamat: 0000-0002-2465-6819

Elena Selli: 0000-0001-8391-7639

Notes

The authors declare no competing financial interest.

■ ACKNOWLEDGMENTS

I.G., M.V.D., and E.S. gratefully acknowledge financial support from Fondazione Cariplo through the 2013-0615 project Novel Photocatalytic Materials Based on Heterojunctions for Solar Energy Conversion and the use of instrumentation purchased through the SmartMatLab project, Fondazione Cariplo Grant 2013-1766. I.G. is thankful to Fondazione Fratelli Confalonieri for a supporting grant. G.C. acknowledges support by the European Union Horizon 2020 Programme under Grant Agreement No. 696656 Graphene Flagship. P.V.K. acknowledges support from the Division of Chemical Sciences, Geosciences, and Biosciences, Office of Basic Energy Sciences of the U.S. Department of Energy through Award DE-FC02-04ER15533. This article is contribution number NRDL 5174 from the Notre Dame Radiation Laboratory.

■ REFERENCES

(1) Park, Y.; McDonald, K. J.; Choi, K.-S. Progress in Bismuth Vanadate Photoanodes for Use in Solar Water Oxidation. *Chem. Soc. Rev.* **2013**, *42*, 2321−2337.

(2) Prévot, M. S.; Sivula, K. Photoelectrochemical Tandem Cells for Solar Water Splitting. *J. Phys. Chem. C* **2013**, *117*, 17879−17893.

(3) Sharp, I. D.; Cooper, J. K.; Toma, F. M.; Buonsanti, R. Bismuth Vanadate as a Platform for Accelerating Discovery and Development of Complex Transition-Metal Oxide Photoanodes. *ACS Energy Lett.* **2017**, *2*, 139−150.

(4) Abdi, F. F.; Han, L.; Smets, A. H. M.; Zeman, M.; Dam, B.; Van de Krol, R. Efficient Solar Water Splitting by Enhanced Charge Separation in a Bismuth Vanadate-Silicon Tandem Photoelectrode. *Nat. Commun.* **2013**, *4*, 1−7.

(5) Zhou, M.; Bao, J.; Xu, Y.; Zhang, J.; Xie, J.; Guan, M.; Wang, C.; Wen, L.; Lei, Y.; Xie, Y. Photoelectrodes Based upon Mo:$BiVO_4$ Inverse Opals for Photoelectrochemical Water Splitting. *ACS Nano* **2014**, *8*, 7088−7098.

(6) Kim, J. H.; Jo, Y.; Kim, J. H.; Jang, J. W.; Kang, H. J.; Lee, Y. H.; Kim, D. S.; Jun, Y.; Lee, J. S. Wireless Solar Water Splitting Device with Robust Cobalt-Catalyzed, Dual-Doped $BiVO_4$ Photoanode and Perovskite Solar Cell in Tandem: a Dual Absorber Artificial Leaf. *ACS Nano* **2015**, *9*, 11820−11829.

(7) Cai, L.; Zhao, J.; Li, H.; Park, J.; Cho, I. S.; Han, H. S.; Zheng, X. One-Step Hydrothermal Deposition of Ni:FeOOH onto Photoanodes for Enhanced Water Oxidation. *ACS Energy Lett.* **2016**, *1*, 624−632.

(8) Hong, S. J.; Lee, S.; Jang, J. S.; Lee, J. S. Heterojunction $BiVO_4$/WO_3 Electrodes for Enhanced Photoactivity of Water Oxidation. *Energy Environ. Sci.* **2011**, *4*, 1781−1787.

(9) Abdi, F. F.; Savenije, T. J.; May, M. M.; Dam, B.; Van de Krol, R. The Origin of Slow Carrier Transport in $BiVO_4$ Thin Film Photoanodes: a Time-Resolved Microwave Conductivity Study. *J. Phys. Chem. Lett.* **2013**, *4*, 2752−2757.

(10) Chatchai, P.; Murakami, Y.; Kishioka, S.; Nosaka, A. Y.; Nosaka, Y. Efficient Photocatalytic Activity of Water Oxidation over WO_3/$BiVO_4$ Composite under Visible Light Irradiation. *Electrochim. Acta* **2009**, *54*, 1147−1152.

(11) Su, J.; Guo, L.; Bao, N.; Grimes, C. A. Nanostructured WO_3/$BiVO_4$ Heterojunction Films for Efficient Photoelectrochemical Water Splitting. *Nano Lett.* **2011**, *11*, 1928−1933.

(12) Shi, X.; Choi, I. Y.; Zhang, K.; Kwon, J.; Kim, D. Y.; Lee, J. K.; Oh, S. H.; Kim, J. K.; Park, J. H. Efficient Photoelectrochemical Hydrogen Production from Bismuth Vanadate-Decorated Tungsten Trioxide Helix Nanostructures. *Nat. Commun.* **2014**, *5*, 4775.

(13) Pihosh, Y.; Turkevych, I.; Mawatari, K.; Uemura, J.; Kazoe, Y.; Kosar, S.; Makita, K.; Sugaya, T.; Matsui, T.; Fujita, D.; et al. Photocatalytic Generation of Hydrogen by Core-Shell WO_3/$BiVO_4$ Nanorods with Ultimate Water Splitting Efficiency. *Sci. Rep.* **2015**, *5*, 11141.

(14) Shi, X.; Jeong, H.; Oh, S. J.; Ma, M.; Zhang, K.; Kwon, J.; Choi, I. T.; Choi, I. Y.; Kim, H. K.; Kim, J. K.; et al. Unassisted Photoelectrochemical Water Splitting Exceeding 7% Solar-to-Hydrogen Conversion Efficiency Using Photon Recycling. *Nat. Commun.* **2016**, *7*, 11943.

(15) Cowan, A. J.; Durrant, J. R. Long-lived Charge Separated States in Nanostructured Semiconductor Photoelectrodes for the Production of Solar Fuels. *Chem. Soc. Rev.* **2013**, *42*, 2281−2293.

(16) Ma, Y.; Mesa, C. A.; Pastor, E.; Kafizas, A.; Francàs, L.; Le Formal, F.; Pendlebury, S. R.; Durrant, J. R. Rate Law Analysis of Water Oxidation and Hole Scavenging on a $BiVO_4$ Photoanode. *ACS Energy Lett.* **2016**, *1*, 618−623.

(17) Ma, Y.; Pendlebury, S. R.; Reynal, A.; Le Formal, F.; Durrant, J. R. Dynamics of Photogenerated Holes in Undoped $BiVO_4$ Photoanodes for Solar Water Oxidation. *Chem. Sci.* **2014**, *5*, 2964−2973.

(18) Ravensbergen, J.; Abdi, F. F.; Van Santen, J. H.; Frese, R. N.; Dam, B.; Van de Krol, R.; Kennis, J. T. M. Unraveling the Carrier Dynamics of $BiVO_4$: a Femtosecond to Microsecond Transient Absorption Study. *J. Phys. Chem. C* **2014**, *118*, 27793−27800.

(19) Ziwritsch, M.; Müller, S.; Hempel, H.; Unold, T.; Abdi, F. F.; Van de Krol, R.; Friedrich, D.; Eichberger, R. Direct Time-Resolved Observation of Carrier Trapping and Polaron Conductivity In $BiVO_4$. *ACS Energy Lett.* **2016**, *1*, 888−894.

(20) Grigioni, I.; Stamplecoskie, K. G.; Selli, E.; Kamat, P. V. Dynamics of Photogenerated Charge Carriers in WO_3/$BiVO_4$ Heterojunction Photoanodes. *J. Phys. Chem. C* **2015**, *119*, 20792−20800.

(21) Pattengale, B.; Huang, J. Implicating the Contributions of Surface and Bulk States on Carrier Trapping and Photocurrent Performance of $BiVO_4$ Photoanodes. *Phys. Chem. Chem. Phys.* **2017**, *19*, 6831−6837.

(22) Di Paola, A.; Palmisano, L.; Venezia, A. M.; Augugliaro, V. Coupled Semiconductor Systems for Photocatalysis. Preparation and Characterization of Polycrystalline Mixed WO_3/WS_2 Powders. *J. Phys. Chem. B* **1999**, *103*, 8236−8244.

(23) Su, J.; Guo, L.; Yoriya, S.; Grimes, C. A. Aqueous Growth of Pyramidal-Shaped $BiVO_4$ Nanowire Arrays and Structural Characterization: Application to Photoelectrochemical Water Splitting. *Cryst. Growth Des.* **2010**, *10*, 856−861.

(24) Aiga, N.; Jia, Q.; Watanabe, K.; Kudo, A.; Sugimoto, T.; Matsumoto, Y. Electron−Phonon Coupling Dynamics at Oxygen Evolution Sites of Visible-Light-Driven Photocatalyst: Bismuth Vanadate. *J. Phys. Chem. C* **2013**, *117*, 9881−9886.

(25) Sivula, K. Metal Oxide Photoelectrodes for Solar Fuel Production, Surface Traps, and Catalysis. *J. Phys. Chem. Lett.* **2013**, *4*, 1624−1633.

DOI: 10.1021/acsenergylett.7b00216
ACS Energy Lett. 2017, 2, 1362−1367